https://doi.org/10.5194/egusphere-2026-246
Preprint. Discussion started: 30 January 2026

Progressive Structural Weakening of the Northern Pine Island Ice Shelf, West Antarctica

Yite Chien[1,2,3], Chunxia Zhou[1,2,3], Baojun Zhang[1,2,3]

[1]Chinese Antarctic Center of Surveying and Mapping, Wuhan University, Wuhan, 430079, China
[2]Key Laboratory of Polar Environment Monitoring and Public Governance (Wuhan University), Ministry of Education, Wuhan, 430079, China
[3]School of Geodesy and Geomatics, Wuhan University, Wuhan, 430079, China

Correspondence to: Chunxia Zhou (zhoucx@whu.edu.cn)

Abstract. The Pine Island Ice Shelf can be analysed within three distinct sectors: northern, southern, and central. Dynamics within the Northern Pine Island Ice Shelf (N-PIIS) remain less understood than those of the Central Pine Island Ice Shelf. Using satellite imagery, reanalysis datasets, and in situ observations, we examined changes in ice-front position, velocity, thickness, rift propagation, and polynya activity across the N-PIIS since 1973. Overall, the ice-shelf area has decreased, and surface elevation data indicate ongoing thinning. Grounded ice velocities have remained largely stable, although localized accelerations occurred near the floating portion of the N-PIIS and the grounded section of Velasco Glacier. Several former pinning points have disappeared, and three polynyas have developed around the ice shelf, suggesting enhanced ocean-ice interaction. Our observations document continued thinning, frontal retreat, pinning-point loss, and episodic polynya formation at the N-PIIS. While large-scale dynamic acceleration is limited, these changes suggest a progressive reduction in structural stability and increased sensitivity to oceanic and atmospheric forcing. This study provides critical new insights into the evolving stability of the N-PIIS and highlights the importance of continued monitoring to anticipate potential disintegration.

1 Introduction

The Pine Island Ice Shelf (PIIS) is one of the most dynamically active ice shelves in West Antarctica and plays a critical role in regulating ice discharge from the Pine Island Glacier basin (Joughin et al., 2021). It is one of the most studied ice shelves in Antarctica (Dirscherl et al., 2020). Previous studies have shown that changes in ice-shelf geometry, grounding, and basal melting strongly influence glacier acceleration and mass loss in this region (Rignot, 2002; Dutrieux et al., 2014). The PIIS is commonly divided into northern, central, and southern sectors, which differ markedly in flow speed, basal melt rates, and buttressing strength (Schmeltz et al., 2001; Rignot, 2002).

Compared with the rapidly thinning and fast-flowing central and southern sectors, the northern PIIS (N-PIIS) has received relatively little attention. The N-PIIS is characterized by slower ice motion and is primarily fed by the Larter, Lucchitta, and Velasco Glaciers (Fig. 1a). Although basal melt rates beneath the N-PIIS are generally lower than those beneath the central ice shelf (Shean et al., 2019; Liu et al., 2024), the region has experienced substantial frontal retreat over recent decades. Between 1966 and 2000, the N-PIIS ice front retreated by more than 25% (Rignot, 2002), and a major calving event in 2015

https://doi.org/10.5194/egusphere-2026-246
Preprint. Discussion started: 30 January 2026

disconnected it from the central PIIS (Arndt et al., 2018). Despite this retreat, the grounding line has remained relatively stable, likely due to local ice rises and rumples that provide partial pinning.

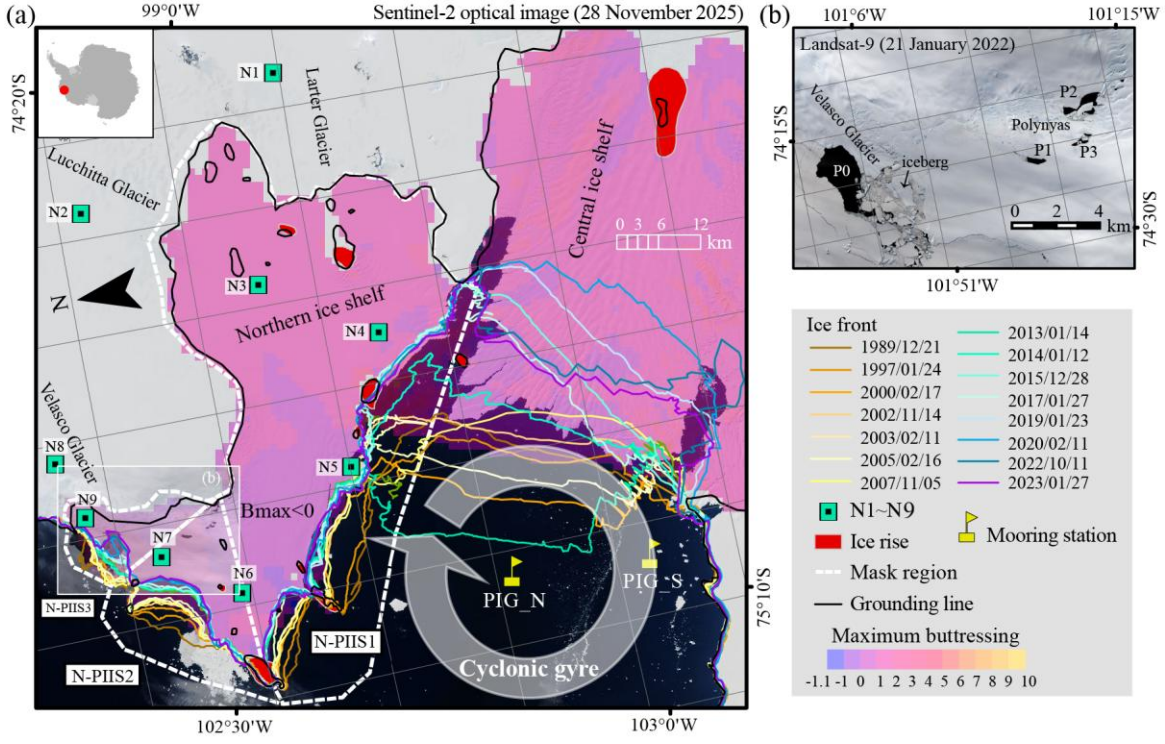

Figure 1. Location and geometry of the N-PIIS. (a) Overview map of the N-PIIS. The background is a Landsat-8 panchromatic image acquired on 28 November 2025, showing the extent of the northern ice shelf and the glaciers feeding into it. N-PIIS1, N-PIIS2, and N-PIIS3 are ice-shelf masks used to calculate area anomalies. Points N1–N9 mark locations where ice velocity time series were extracted. The ice front positions were delineated from Landsat optical and Sentinel-1 SAR images, following Chien et al. (2025a, b). The grounding line (black) is from Rignot et al. (2016). Ice rises and rumples (red) are from Moholdt and Matsuoka (2015). The colour scale indicates maximum buttressing from Durand et al. (2016); areas with maximum buttressing values below zero are shown in purple and outlined in red. PIG-N and PIG-S denote hydrographic mooring sites located in front of the PIIS. The large semi-transparent white circle with arrows indicates the approximate size and location of the cyclonic gyre in Pine Island Bay (PIB), based on Yoon et al. (2022). White frame with semi-transparent Landsat-9 image represent the region in panel (b). (b) Subregion showing the Velasco Glacier and polynyas. The background image is a Landsat-9 image acquired on 21 January 2022.

Recent studies have demonstrated that ice-shelf thinning and pinning-point loss can precede rapid structural weakening and collapse, as observed for the Conger–Glenzer Ice Shelf in East Antarctica (Walker et al., 2024). Rignot (2002) also reported reductions in pinning-point extent at the N-PIIS. This observation raises the hypothesis that processes similar to those identified at the Conger–Glenzer Ice Shelf may also be occurring at the N-PIIS, although this possibility requires further investigation. The mechanisms driving these changes, and their potential links to oceanic and atmospheric forcing, remain poorly understood.

Polynyas are increasingly recognized as indicators of ocean–ice–atmosphere interactions near Antarctic ice shelves. At Pine Island Glacier, polynyas near the central ice-shelf front have been linked to basal melting, ocean circulation, and atmospheric

https://doi.org/10.5194/egusphere-2026-246
Preprint. Discussion started: 30 January 2026

forcing (Mankoff et al., 2012; Savidge et al., 2023a, 2023b). In contrast, a series of polynyas observed within the N-PIIS, distinct from those forming in the surrounding sea ice, have not been systematically documented or analysed (Fig. 1b). The formation mechanisms and historical evolution of these features have not yet been documented, underscoring the need for further investigation.

Here we present an observation-based analysis of recent structural and dynamic changes of the N-PIIS. Rather than attributing changes to a single forcing mechanism, we document co-evolving ice-front retreat, grounding conditions, thinning signals, and polynya occurrence, and discuss their consistency with oceanic and atmospheric influences. We focus on three key phenomena: (1) ice-front retreat; (2) the evolution of rifting and pinning points across the N-PIIS; and (3) the occurrence of anomalous polynyas and associated ice thinning. Together, these observations provide new insights into the evolving stability of the N-PIIS and its susceptibility to future structural weakening.

2. Data and Methods

2.1 Ice-front position, rift propagation, and polynya mapping

Landsat and Sentinel-1/2 imagery accessed via USGS EarthExplorer, the Copernicus Browser, and Google Earth Engine were used to analyse ice-front position changes, rift propagation, and polynya formation at the N-PIIS. Ice-front positions were manually delineated from 1997 to 2025 using Landsat panchromatic images (15 m spatial resolution) and Sentinel-1 IW GRD images (10 m spatial resolution). The positional uncertainty of the extracted ice front is estimated to be ±1 pixel along the entire ice-front length.

Changes in ice-front position were quantified relative to a reference ice-shelf mask. Ice-shelf masks for N-PIIS1, N-PIIS2, and N-PIIS3 (Fig. 1) were defined using the 2011 grounding line (Rignot et al., 2016) and were extended beyond the observed ice-shelf extent to ensure complete capture of frontal variation. Ice-shelf area anomalies were calculated by subtracting the mean area of the full time series from each individual observation.

Landsat-7/8/9 optical imagery (30 m spatial resolution), Sentinel-2 optical imagery (10 m spatial resolution), and Sentinel-1 SAR imagery (10 m spatial resolution) were further used to document polynya evolution in 2021, an anomalous thinning episode during the austral winter of 2024, and rift propagation in 2025.

2.2 Ice velocity

Ice velocity and uncertainty data were obtained from the velocity product developed by Chien et al. (2025a, b), which is based on offset tracking of Sentinel-1 IW imagery from October 2014 to August 2025. Velocity time series were extracted at nine locations (N1–N9; Fig. 1). Sites N1 and N2 are located on the grounded Larter and Lucchitta Glaciers, respectively; sites N3–

https://doi.org/10.5194/egusphere-2026-246
Preprint. Discussion started: 30 January 2026

N7 are situated on the floating ice shelf; and sites N8–N9 are located on the Velasco Glacier. Velocity with uncertainty larger than 0.25 m day^{-1} or lower than -0.25 m day^{-1} was excluded.

2.3 Grounding line and pinning points

Grounding-line position and pinning-point evolution were examined using the double-differential InSAR (DDInSAR) technique (Rignot et al., 2011). DDInSAR interferograms were generated from three-pass Sentinel-1A/B IW acquisitions with a 6-day repeat cycle between 2017 and 2020. Assuming constant ice velocity over the temporal baseline, the resulting interferograms isolate tidal flexure signals at the grounding zone, which appear as dense fringe belts. The landward limit of the fringe belt was manually digitized as the grounding line, while changes in fringe geometry were used to identify the appearance or disappearance of pinning points. All interferograms were geocoded using the REMA 200 m digital elevation model and analysed at a 20 m grid spacing (Howat et al., 2019, 2022).

2.4 Surface elevation

Surface elevation changes were assessed using ICESat-2 ATL06 land-ice height data (Smith et al., 2019, 2023) from 2018 to 2023. A single repeat track (track 1026) crossing the N-PIIS and adjacent polynya regions was analyzed. Heights were converted to elevations relative to the EGM2008 geoid and applying ocean tide and dynamic atmospheric corrections following Wang et al. (2021).

2.5 Atmospheric forcing

Atmospheric conditions were analyzed using hourly ERA5 reanalysis data (Hersbach et al., 2023), including 2 m air temperature, 2 m relative humidity, and 10 m wind speed. Data were extracted over a region spanning 75°–74.5°S and 102.25°–101.5°W, encompassing the N-PIIS and adjacent polynya areas. Relative humidity was calculated from 2 m air temperature and 2 m dewpoint temperature using the August–Roche–Magnus approximation.

Foehn wind events were identified using a threshold-based approach following Laffin et al. (2021) and Francis et al. (2023). Events were defined when 2 m air temperature and 10 m wind speed exceeded the 60th percentile, 2 m relative humidity exceeded the 30th percentile, with thresholds calculated over the full study period (September 2021–February 2022 and June 2024–October 2024). Typical ERA5 biases for 2 m air temperature, 2 m relative humidity, and 10 m wind speed in Antarctica are approximately 0.5–1.5 °C, 5–10%, and 0.5–1.5 m s^{-1}, respectively (Gossart et al., 2019; Francis et al., 2023).

2.6 Ocean observation

Ocean temperature and salinity time series were obtained from the PIG-N and PIG-S moorings (Fig. 1), which provide measurements at depths between 300 and 700 m below mean sea level from 2016 to 2024 (Zhou et al., 2024, 2025).

https://doi.org/10.5194/egusphere-2026-246
Preprint. Discussion started: 30 January 2026

3. Results

3.1 Area and ice velocity changes at the N-PIIS

The ice fronts of the N-PIIS and the Velasco Glacier experienced multiple phases of retreat since 1973 (Fig. 1). In the N-PIIS1 region, the largest area loss occurred between 2014 and 2015, totalling approximately 200 km², coinciding with the disconnection from the central ice shelf. In the N-PIIS2 region, the ice-shelf area decreased by about 60 km², while the N-PIIS3 region showed a more pronounced retreat after 2007, with a total loss of approximately 20 km² (Fig. 2a).

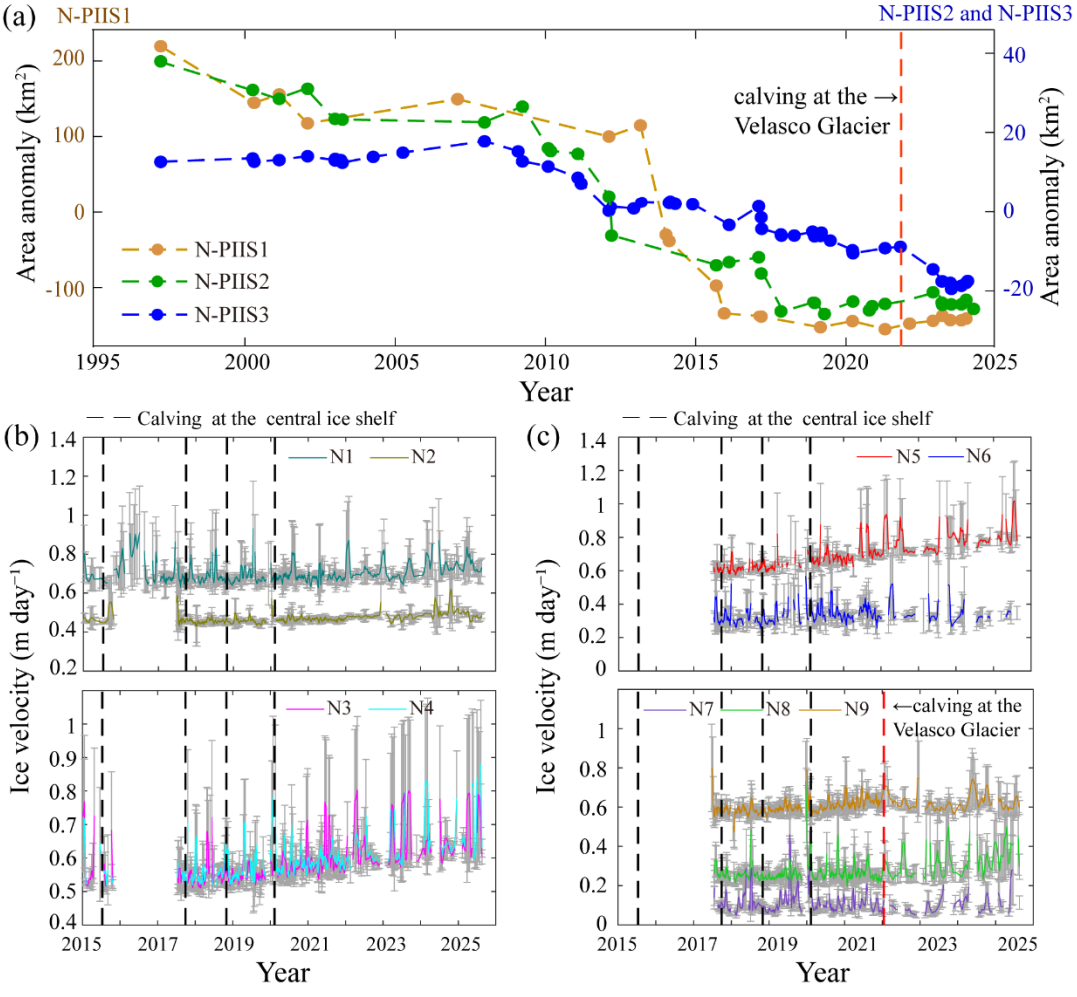

Figure 2. Area anomalies and ice velocity changes at the N-PIIS. (a) Area anomaly time series from 1997 to 2025. (b) Ice velocity time series with associated uncertainties at locations N1–N4. (c) Ice velocity time series with associated uncertainties at locations N5–N9. Dash lines represent calving events. Black dash lines represent calving events happened at the central ice shelf. Red dash line represented calving event happened at the Velasco Glacier.

Ice-velocity time series at locations N1 (Larter Glacier) and N2 (Lucchitta Glacier), situated within grounded ice regions, remained below 1.5 m day⁻¹ with no significant changes. At positions N3–N5, a slight increase in ice velocity was observed (Fig. 2b, c). Ice velocity increased following the major calving event at Velasco Glacier in January 2022 at location N8, which

https://doi.org/10.5194/egusphere-2026-246
Preprint. Discussion started: 30 January 2026

is located upstream of the grounding line (Fig. 2c). The 2022 calving event at Velasco Glacier occurred between 14 and 17 January 2022 (Fig. 3). Rift was observed in late September 2021, coinciding with the formation of melt ponds on the fast ice, which developed into polynya P0. An expansion of polynya P0, together with the formation of new rifts within the fast ice, was observed on 10 November 2021. Fast-ice breakup progressed by 28 November 2021, extending toward the ice tongue, and fully disintegrated was observed by 20 December. The calving event ultimately detached an iceberg approximately 3.50 km², reducing the ice tongue length by about 30%.

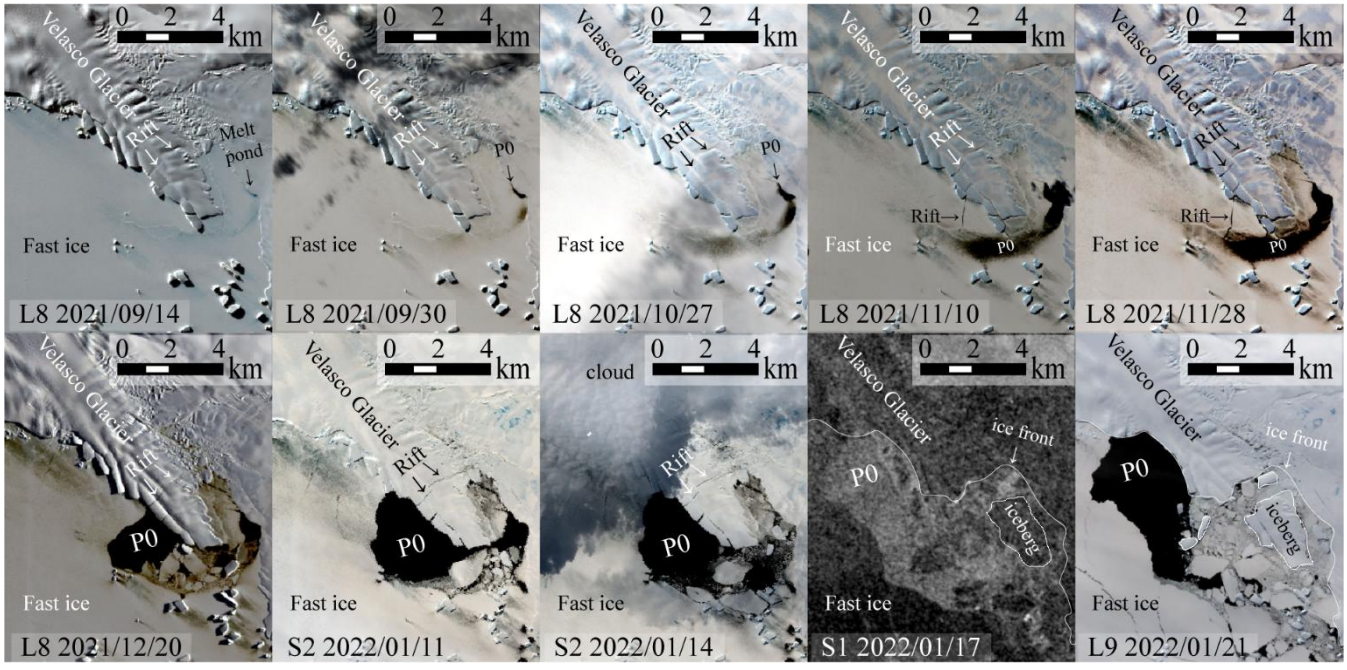

Figure. 3. The 2022 calving event at the Velasco Glacier as documented by Landsat-8/9 and Sentinel-1/2 imagery from September 2021 to January 2022.

3.2 Observation of pinning point changes and rift propagation at the N-PIIS

The interferograms show stable fringe patterns over time, while revealing the disappearance of pinning points E1, E2, E3, and E6, and the emergence of a new pinning point E9, with a new rift forming adjacent to it (Fig. 4a, b). This new rift was observed in Sentinel-2 optical imagery from November 2025 and Sentinel-1 SAR imagery from August to September 2025 (Fig. 3c-e). The interferograms also show that the Velasco Glacier was grounded in 2019 (Fig. 4a) and largely ungrounded in October 2025 (Fig. 4b).

https://doi.org/10.5194/egusphere-2026-246
Preprint. Discussion started: 30 January 2026

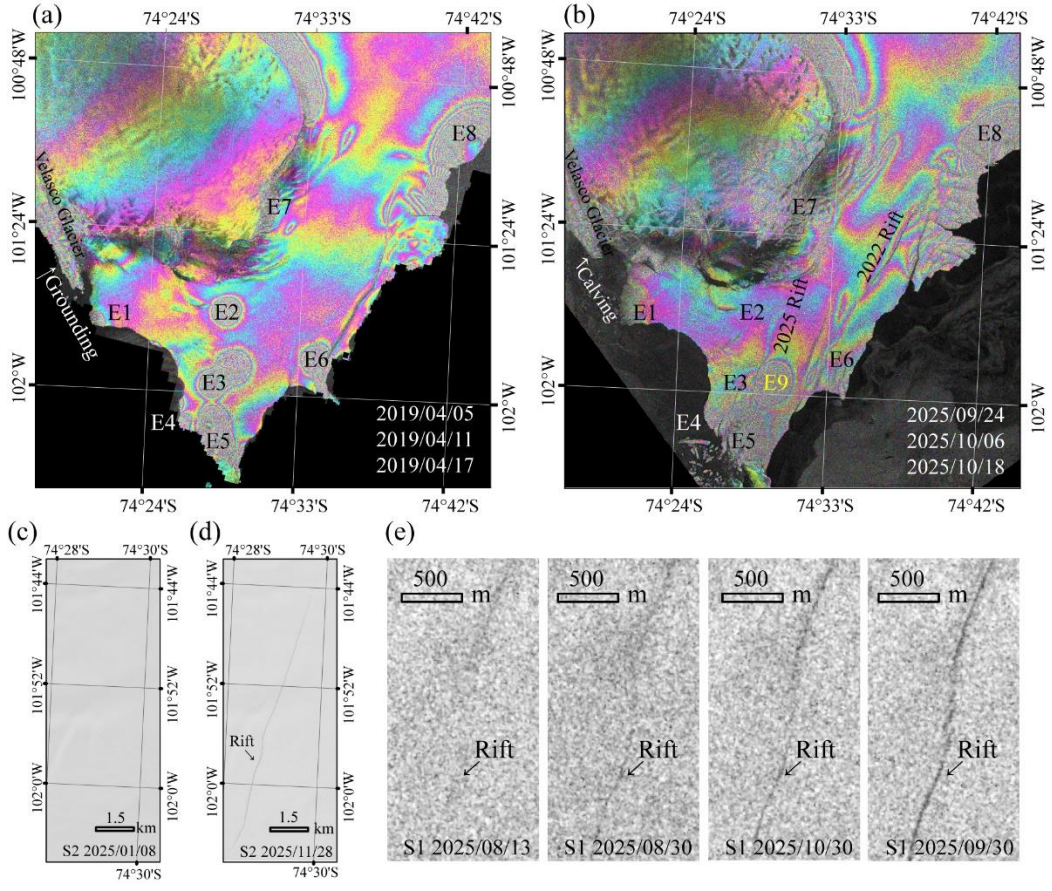

Figure 4. DDInSAR interferograms and evolution of rift propagation at the N-PIIS. (a–b) DDInSAR interferograms acquired in April 2019 and October 2025. (c-d) Sentinel-2 optical images acquired on 8 January 2025 and 28 November 2025 respectively. (e) Rift propagation history from 13 August to 30 September 2025 derived from Sentinel-1 SAR imagery.

3.3 Polynya formation in 2021 and the thinning of the N-PIIS in 2024

Three recurrent polynyas (P1–P3) were identified within the N-PIIS region (Fig. 5a). Polynya P1 formed in 2019, expanded in 2021, and reappeared in 2023 (Figure 5c). Polynya P2 was observed in 2003, 2005, 2007, 2019, 2021, 2022, and 2023 (Fig. 5d). The area of P2 was larger in 2005 and 2021, coinciding with years when fast-ice fully covered the PIB (Fig. 5b). Polynya P3 was observed in 2021/2022 austral summer (Fig. 5e). Analysis of foehn wind activity from September 2021 to February 2022 revealed eight events around 31 October 2021 and five additional events between December 2021 and February 2022 (Fig. 5f). The higher frequency of foehn winds in late October 2021 coincided with polynyas formation by 10 November 2021 (Fig. 5c–e).

https://doi.org/10.5194/egusphere-2026-246
Preprint. Discussion started: 30 January 2026

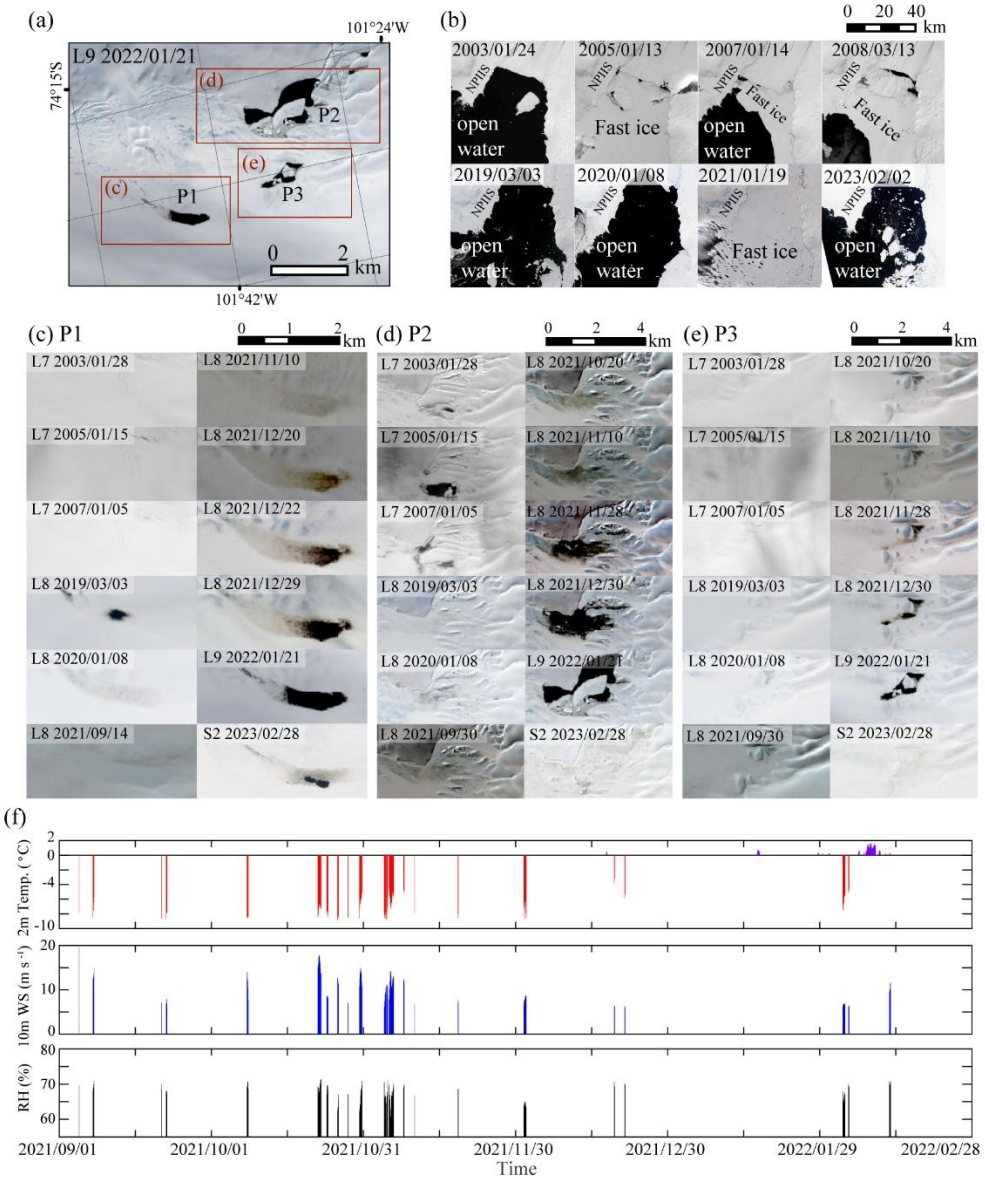

Figure 5. Formation of polynyas in the N-PIIS, sea-ice coverage in PIB from 2003 to 2023, and time series of temperature, wind speed, and relative humidity. (a) Overview map showing the locations of polynyas P1–P3. (b) Sea-ice coverage in PIB from 2003 to 2023. (c–e) Formation and evolution of polynyas P1–P3 from 2003 to 2023. (f) Time series of 2-m air temperature (2m Temp.), 10-m wind speed (10m WS), and relative humidity (RH) from September 2021 to February 2022.

During the 2024 austral summer, the PIB was covered by fast ice, consistent with Sentinel-2 imagery from 24 September 2024 (Fig. 6a). During the same period in 2024, Sentinel-1 IW imagery from June to November 2024 shows progressive darkening in a region over six months (Fig. 6b). Sentinel-2 optical images from 24 September and 30 October 2024 show that this region remained covered by fast ice, indicating that the observed darkening in SAR imagery corresponds to ice thinning rather than

https://doi.org/10.5194/egusphere-2026-246
Preprint. Discussion started: 30 January 2026

new polynya formation (Fig. 6b). Meteorological data from June to October 2024 indicate multiple wind events (Fig. 6c). However, during the foehn wind events, the SAR image time series show gradual changes in the extent of the darkened region (indicated by the yellow arrow, Fig. 6b), suggesting that factors other than foehn winds may have contributed to the observed thickness changes in the 2024 austral summer.

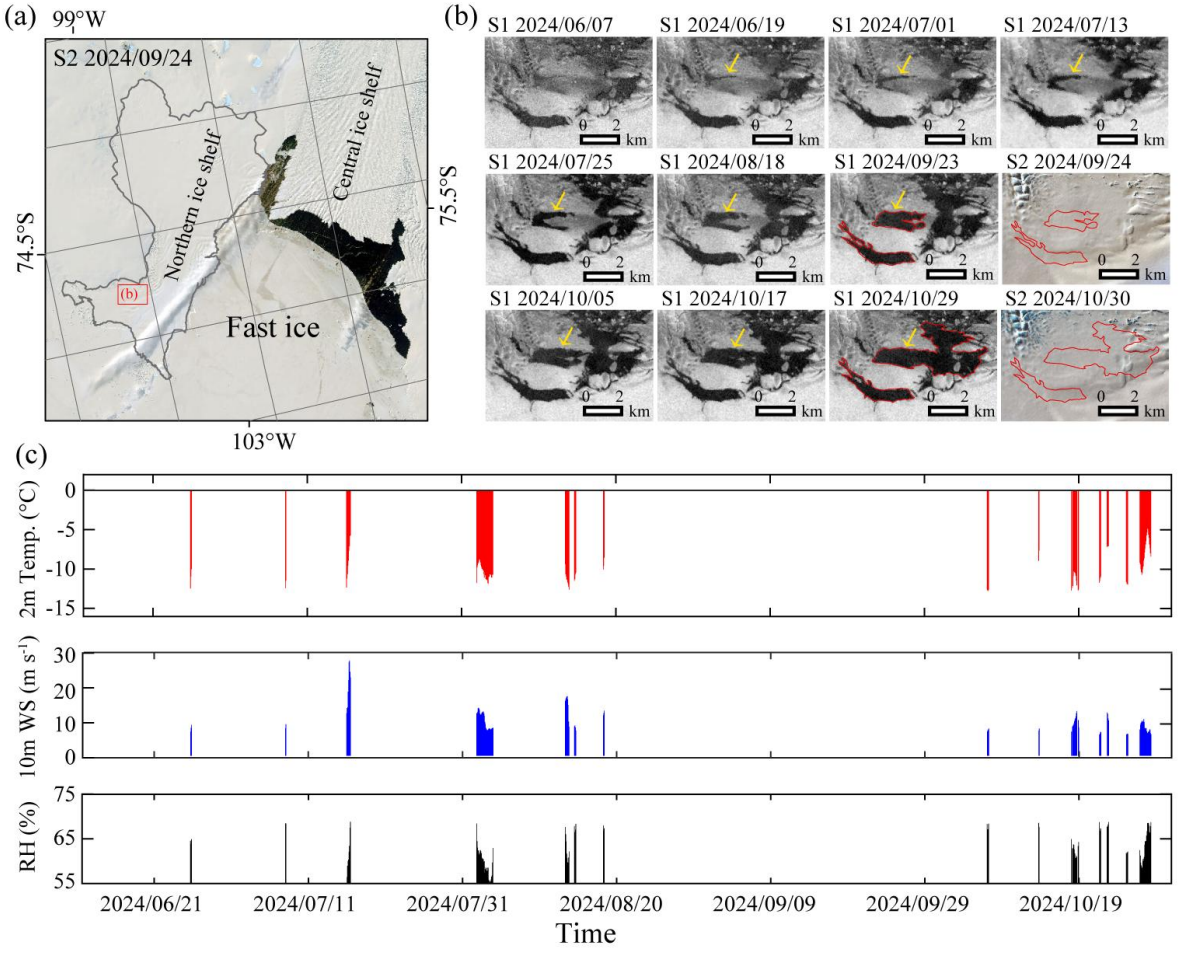

Figure 6. Sentinel-1 images of the region near the P2 polynya, sea-ice coverage in the PIB in 2024, and time series of temperature, wind speed and relative humidity. (a) Sea-ice coverage in the PIB in 24 September 2024. (b) Sentinel-1 images showing ice thinning between June and November 2024, compared with Sentinel-2 optical images acquired on 24 September and 30 October 2024. Yellow arrows indicate the thinning region; red outlines mark melt areas detected in SAR imagery. (c) Time series of 2m Temp., 10m WS, and RH from June to October 2024.

ICESat-2 surface elevation data indicate a general decrease in elevation across the N-PIIS between 2019 and 2023 (Fig. 7). Over the Velasco Glacier, surface elevations ranged between 30 and 40 m near the grounded region (Fig. 7b, pink blocks) and ranged around 25 m near the ice front (Fig. 7c, orange block). In the polynya P2 and adjacent regions, surface elevations were close to 0 m (Fig. 7a, c, green block). Surface elevations near polynyas P1 and P3 decreased during this period (Fig. 7d, blue block).

https://doi.org/10.5194/egusphere-2026-246
Preprint. Discussion started: 30 January 2026

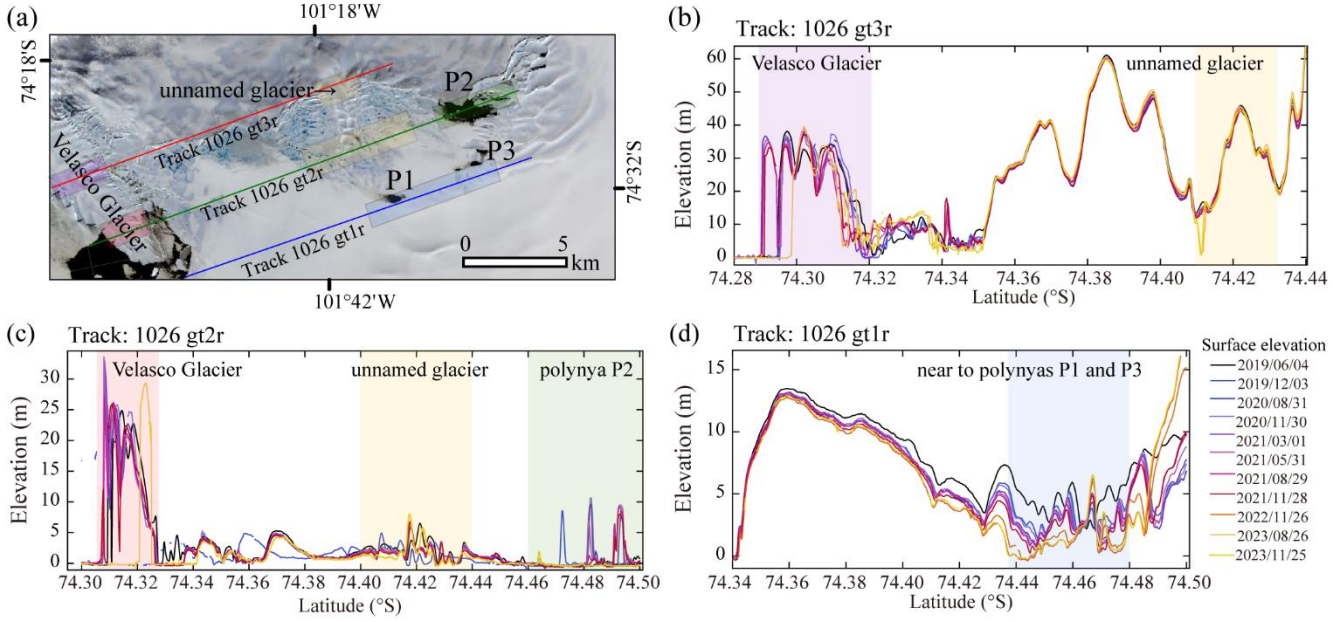

Figure 7. Surface elevation along ICESat-2 track 1026 near the Velasco Glacier. (a) Locations of the three strong beams of ICESat-2 track 1026 (gt1r, gt2r, and gt3r). (b) Surface elevation profiles along sub-track gt3r beam between latitudes 74.28°S and 74.44°S. (c-d) Surface elevation profiles along sub-tracks gt2r and gt1r between latitude74.30°S and 74.50°S. Coloured blocks in (b-d) highlight the ice profiles of the Velasco Glacier (pink and orange), the unnamed glacier (yellow), and the surrounding polynya regions (green and blue) shown as coloured panels in (a).

Surface elevation data from Copernicus DEM indicate an average elevation of approximately 50 m across the N-PIIS, with the thickest ice near the Lucchitta and Larter Glaciers (Fig. 8a). The northern sector, particularly near polynyas P1–P3, is thinnest, with surface elevations below 10 m (Fig. 7c, 8a). Bed elevations in this region are approximately 300 m below sea level (Fig. 8b). Two major troughs are present beneath the northern ice shelf.

https://doi.org/10.5194/egusphere-2026-246
Preprint. Discussion started: 30 January 2026

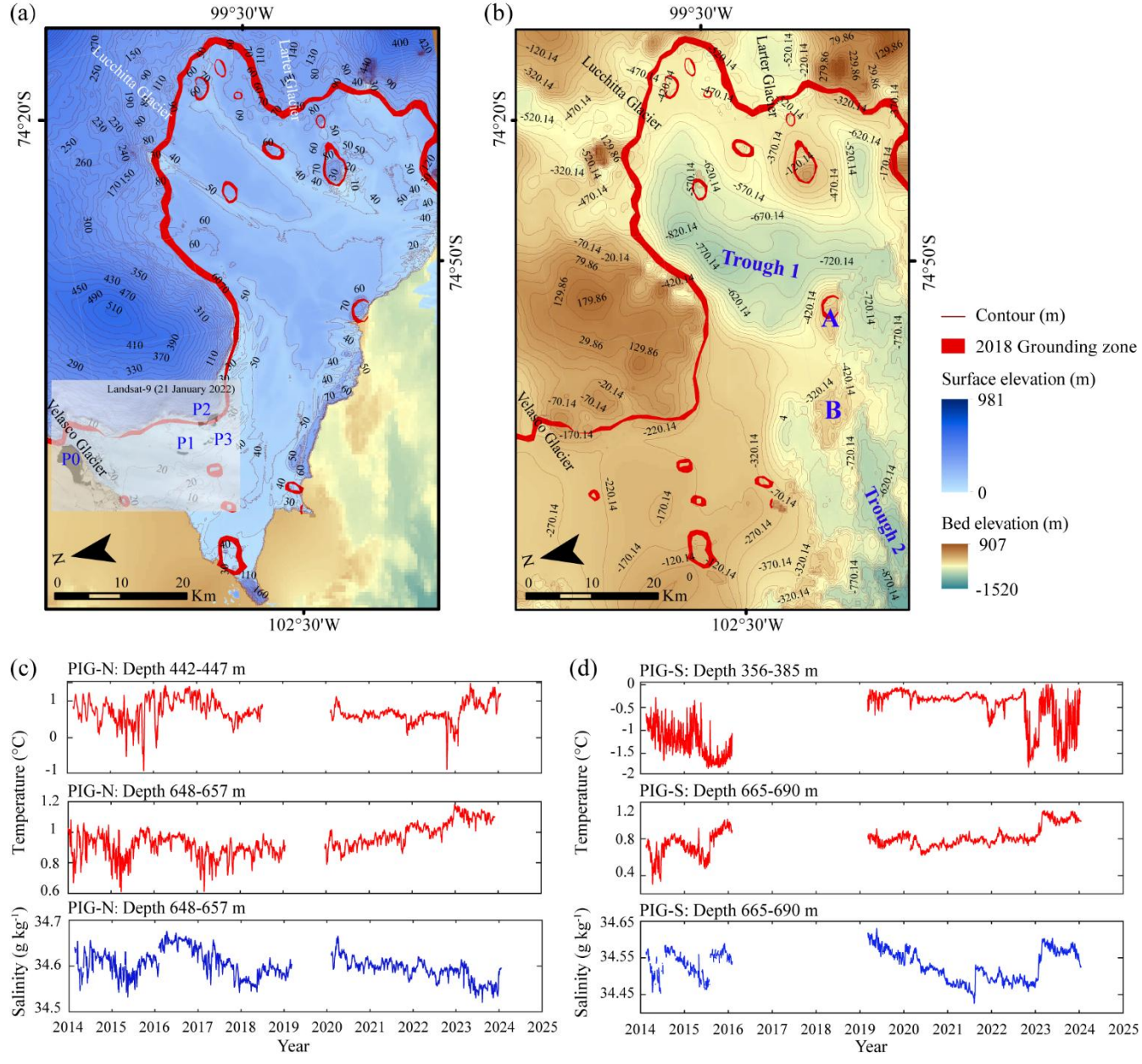

185 **Figure 8. Topography of the N-PIIS and oceanic parameters of the PIG-N and PIG-S moorings. (a) Surface elevation from the Copernicus DEM. The Landsat-9 image acquired on 21 January 2022 reveals the positions of polynyas P0–P3. (b) Bed elevation from BedMachine v3 (Morlighem et al., 2020; Morlighem, 2022). The red band marks the 2018 grounding zone (Rignot et al., 2023). A and B denote seafloor ridges. (c-d) Ocean temperature and salinity time series from 2014 to 2024 at the PIG-N and PIG-S moorings, respectively.**

190 Oceanographic observations from mooring stations show temperature and salinity variations from 2014 to 2024 (Fig. 7c, d). At PIG-N, temperatures at 442–447 m increased after 2023, while temperatures at 648–657 m rose between 2020 and 2023, accompanied by decreasing salinity. At PIG-S, temperatures at 356–385 m remained near 0°C after 2019, with cooling events

https://doi.org/10.5194/egusphere-2026-246
Preprint. Discussion started: 30 January 2026

at the ends of 2022 and 2023. Temperatures at 665–690 m increased by ~0.2°C in 2023, stabilizing near 1°C, with salinity exceeding 34.55 g kg^{-1}. Data gaps between 2016 and 2019 prevent precise determination of the warming onset.

4. Discussion

4.1 Structural evolution and ice-dynamic response of the N-PIIS

Our observations indicate that the N-PIIS is undergoing progressive structural weakening, characterized by frontal retreat, rifting, and the loss of multiple pinning points, while exhibiting only modest changes in ice velocity across most of the shelf. Ice velocity time series show that grounded ice at the Lucchitta and Larter Glaciers remained largely stable throughout the study period, consistent with the limited buttressing provided by the northern ice shelf, where maximum buttressing values are low or negative (Fig. 1). This explains why large-scale retreat of the N-PIIS has not translated into widespread acceleration of upstream grounded ice.

Localized accelerations observed at sites N3 and N6 likely reflect a delayed dynamic response to the 2015 calving event that disconnected the N-PIIS from the central Pine Island Ice Shelf (Fig. 2b, c). In contrast, the marked acceleration at site N8 is directly associated with the area decreased within N-PIIS3 and partial ungrounding of the Velasco Glacier (Fig. 2c, 3, 4a, 4b). The loss of floating ice and grounding at the Velasco Glacier front likely reduced local resistive stresses, allowing increased flow speeds upstream of the former grounding zone (Fig. 4a, b). This spatially heterogeneous velocity response highlights the importance of grounding conditions and local geometry in controlling ice dynamics within the N-PIIS system.

Independent evidence from ICESat-2 surface elevation data and DDInSAR interferograms demonstrates sustained thinning of the N-PIIS between 2018 and 2023 (Figs. 4a, 4b, 7c). The disappearance of pinning points E1, E2, E3, and E6, together with the emergence of a new pinning point E9 adjacent to an actively propagating rift, indicates significant reorganization of ice–bed interactions (Fig. 4a, b). Such changes are consistent with gradual thickness reduction that weakens grounding at former pinning points while allowing new, transient contacts to form where ice geometry permits.

Pinning-point loss reduces local buttressing and can promote rift initiation and propagation by altering the stress regime within the ice shelf (Arndt et al., 2018). The spatial coincidence of rift development with evolving pinning points suggests that thinning-driven changes in basal contact play a key role in controlling fracture patterns across the N-PIIS (Fig. 4c). Although grounding-line migration remains limited, these observations indicate that the ice shelf is becoming increasingly sensitive to further thinning and mechanical perturbations.

https://doi.org/10.5194/egusphere-2026-246
Preprint. Discussion started: 30 January 2026

4.2 Links between ocean forcing, atmospheric forcing and polynya occurrence

The formation of polynyas within and adjacent to the N-PIIS provides additional insight into the processes driving ice-shelf thinning. Bathymetric data reveal troughs extending beneath the northern ice shelf that may permit episodic access of mCDW to the ice-shelf base (Fig. 8b). Ocean temperature records from nearby moorings show warming at intermediate and deep depths after 2020–2023 (Fig. 8c, d), which may have enhanced the intrusion of warm water beneath the ice shelf and increased basal melting.

The polynyas P1–P3 do not occur annually, indicating that basal melting alone is insufficient to explain their formation (Fig. 4). Atmospheric forcing, particularly foehn wind events, likely acts as a secondary trigger by promoting surface melt or weakening fast ice, thereby facilitating polynya opening during periods of elevated ocean heat flux. For example, the high frequency of foehn events in late October 2021 preceded polynya formation in early November, suggesting that atmospheric conditions contributed to initiating open-water or thin-ice areas (Fig. 5). In contrast, during the austral winter of 2024, gradual thinning detected in SAR imagery occurred without rapid surface opening, implying a stronger contribution from sustained basal melting rather than short-lived atmospheric forcing (Fig. 6).

Sea-ice conditions in the PIB appear to further modulate these processes. Periods of persistent fast-ice cover the whole PIB, such as in 2005 and 2021, coincide with particularly large polynya extents within the N-PIIS (Fig. 5). Extensive fast ice may suppress surface heat loss and weaken local circulation (PIB gyre), thereby enhancing heat retention at depth and increasing basal melt rates beneath the ice shelf (Zheng et al., 2021; Dotto et al., 2022; Yoon et al. 2022; Wild et al., 2025). These interactions highlight the coupled influence of oceanic heat supply, sea-ice conditions, and atmospheric forcing on polynya variability and ice-shelf thinning.

4.3 Implications for future stability of the N-PIIS

The observed combination of thinning, pinning-point loss, and rift development suggests that the N-PIIS is transitioning toward a more vulnerable structural state. While large-scale dynamic collapse is not imminent, the progressive reduction in thickness and basal contact reduces the stabilizing influence of pinning points and increases the likelihood of further rifting and calving. Similar sequences of long-term thinning followed by structural weakening have been documented prior to the collapse of other Antarctic ice shelves, such as the Conger–Glenzer Ice Shelf in East Antarctica (Walker et al., 2024) and the Wordle Ice Shelf in the Antarctic Peninsula (Dømgaard et al., 2025).

Continued ocean warming, combined with episodic atmospheric forcing and persistent fast-ice fully covering over the PIB, may further enhance basal melting and fracture propagation at the N-PIIS. Sustained satellite monitoring, together with targeted in situ observations and modelling, will be essential to assess whether the N-PIIS is approaching a threshold beyond which rapid structural change becomes unavoidable.

https://doi.org/10.5194/egusphere-2026-246
Preprint. Discussion started: 30 January 2026

5. Conclusion

Using satellite imagery, reanalysis datasets, and in situ observations, we examined recent changes in the N-PIIS. Our results reveal the ongoing structural weakening of the N-PIIS and clarifies the mechanisms linking ice-shelf thinning, grounding conditions, and external forcing. Since 1973, the area of the N-PIIS has decreased. Ice velocities across the N-PIIS have remained largely stable. However, localized accelerations are observed in the grounded section of the Velasco Glacier, reflecting reduced ice-tongue buttressing following the 2022 calving event and the resulting increase in grounded ice velocity. Surface elevation data show continued thinning, and several pinning points have disappeared. We also documented the formation of three polynyas surrounded by the N-PIIS. These observations indicate that the N-PIIS is not fully stable. Although rapid collapse is not imminent, continued ocean warming and episodic atmospheric forcing may accelerate structural degradation. Continued monitoring through satellite imagery, targeted in situ observations, and modelling will be essential to evaluate whether ongoing thinning, calving, and rifting may lead to more rapid structural changes in the future.

Code and data availability: All software (except GAMMA, which is commercial software and was used to generate ice velocity and DDInSAR interferograms), codes, and satellite and climate datasets used in this study are publicly available and can be obtained from the following sources: Processed area shape files, ICESat-2 data, and related MATLAB scripts for plotting Figure 2 and Figure 6 are available from Zenodo (Chien, 2026). The MATLAB plotting codes on which this article is based are available in Greene et al (2017) and Greene (2021). REMA 200 m DEM mosaic is available from Howat et al. (2022). Ice front positions were delineated from Landsat optical imagery and Sentinel-1 SAR data, and are available from Zenodo (Chien et al. 2025b). Grounding line positions were obtained from NSIDC (Rignot et al., 2016). Ice rises and rumples were sourced from the Norwegian Polar Institute (Moholdt and Matsuoka, 2015). Ice-shelf buttressing data are available from NSIDC (Durand et al., 2016). Optical and SAR imagery from Landsat, Sentinel-1, and Sentinel-2 were accessed via USGS EarthExplorer (https://earthexplorer.usgs.gov/, last access: 15 January 2026), Google Earth Engine (https://earthengine.google.com/, last access: 15 January 2026), and the Copernicus Data Space Browser (https://browser.dataspace.copernicus.eu/, last access: 15 January 2026). ICESat-2 ATL06 surface elevation data are available from NSIDC (Smith et al., 2023). Atmospheric variables (10-m wind speed and 2-m air temperature) were obtained from ERA5 hourly reanalysis via ECMWF Climate Data Store (Hersbach et al., 2023). Ocean temperature time series at PIG-N and PIG-S moorings are available in NetCDF format from SEANOE (Zhou et al., 2024). Bed elevations for the N-PIIS were obtained from BedMachine v3 (Morlighem, 2022), and the 2018 grounding zone is available from Rignot et al. (2023). The Sentinel-1 image IDs can be accessed in Supplementary Tables S1.

Author contribution: YC and ZC designed the experiments and YC developed the MATLAB code and performed all the experiments. YC prepared the manuscript supervised from ZC and ZB.

Acknowledgements: The authors thank the organizations and projects listed in the Data Availability section for providing essential datasets. We are also grateful to the anonymous reviewers and the scientific editor for their constructive comments, which greatly improved the manuscript.

Financial support: This research was supported by the National Natural Science Foundation of China (Grants 42171133 and 41941010) and the Fundamental Research Funds for the Central Universities (Grant 2042024kf0016).

https://doi.org/10.5194/egusphere-2026-246
Preprint. Discussion started: 30 January 2026

References

Arndt, J. E., Larter, R. D., Friedl, P., Gohl, K., Höppner, K., and the Science Team of Expedition PS104: Bathymetric controls on calving processes at Pine Island Glacier, The Cryosphere, 12, 2039–2050, https://doi.org/10.5194/tc-12-2039-2018, 2018.

Chien, Y., Zhou, C., and Riel, B.: Mélange-driven coupling between the central Pine Island Ice Shelf and the Piglet Glacier reverses recent acceleration trends, Geophys. Res. Lett.,52, e2025GL119556, https://doi.org/10.1029/2025GL119556, 2025a.

Chien, Y., Zhou, C., and Riel, B.: Datasets for the study “Mélange-driven coupling between the central Pine Island Ice Shelf and Piglet Glacier reverses recent acceleration trends”, Zenodo [dataset], https://zenodo.org/uploads/17722558 (last access: 15 January 2026), 2025b.

Chien, Y.: Dataset for the manuscript "Progressive Structural Weakening of the Northern Pine Island Ice Shelf, West Antarctica", [Dataset]. Zenodo. https://doi.org/10.5281/zenodo.18266529 (last access: 16 January 2026), 2026.

Dirscherl, M., Dietz, A. J., Dech, S., and Kuenzer, C.: Remote sensing of ice motion in Antarctica – a review, Remote Sens. Environ., 237, 111595, https://doi.org/10.1016/j.rse.2019.111595, 2020.

Dømgaard, M., Millan, R., Andersen, J. K., et al.: Half a century of dynamic instability following the ocean-driven break-up of Wordie Ice Shelf, Nat. Commun., 16, 4016, https://doi.org/10.1038/s41467-025-59293-1, 2025.

Dotto, T. S., Heywood, K. J., Hall, R. A., Scambos, T. A., Zheng, Y., Nakayama, Y., et al.: Ocean variability beneath Thwaites Eastern Ice Shelf driven by the Pine Island Bay Gyre strength, Nat. Commun., 13, 7840, https://doi.org/10.1038/s41467-022-35455-x, 2022.

Durand, G., Gillet-Chaulet, F., Gagliardini, O., and Fürst, J. J.: SUMER Antarctic Ice-shelf Buttressing (NSIDC-0664, Version 1), NASA NSIDC DAAC [dataset], https://doi.org/10.5067/FWHORAYVZCE7(last access: 15 January 2026), 2016.

Dutrieux, P., De Rydt, J., Jenkins, A., Holland, P. R., Ha, H. K., Lee, S. H., et al.: Strong sensitivity of Pine Island ice-shelf melting to climatic variability, Science, 343, 174–178, https://doi.org/10.1126/science.1244341, 2014.

Francis, D., Fonseca, R., Mattingly, K. S., Lhermitte, S., and Walker, C.: Foehn winds at Pine Island Glacier and their role in ice changes, The Cryosphere, 17, 3041–3062, https://doi.org/10.5194/tc-17-3041-2023, 2023.

Gossart, A., Helsen, J., Lenaerts, J. T. M., Vanden Broucke, S., van Lipzig, N. P. M., and Souverijns, N.: An evaluation of surface climatology in state-of-the-art reanalyses over the Antarctic Ice Sheet, J. Climate, 32, 6899–6915, https://doi.org/10.1175/JCLI-D-19-0030.1, 2019.

https://doi.org/10.5194/egusphere-2026-246
Preprint. Discussion started: 30 January 2026

Greene, C. A., Gwyther, D. E., and Blankenship, D. D.: Antarctic mapping tools for MATLAB, Comput. Geosci., 104, 151–157, https://doi.org/10.1016/j.cageo.2016.08.003, 2017.

Greene, C. A.: Antarctic Mapping Tools, Version 6, [Software], GitHub, https://github.com/chadagreene/Antarctic-Mapping-Tools (last access: 15 January 2026), 2021.

315 Hersbach, H., Bell, B., Berrisford, P., et al.: ERA5 hourly data on single levels from 1940 to present, Copernicus Climate Change Service (C3S) Climate Data Store [dataset], https://doi.org/10.24381/cds.adbb2d47 (last access: 15 January 2026), 2023.

Howat, I., Porter, C., Smith, B. E., Noh, M. J., and Morin, P.: The reference elevation model of Antarctica, The Cryosphere, 13, 665–674, https://doi.org/10.5194/tc-13-665-2019, 2019.

320 Howat, I., Porter, C., Noh, M., Husby, E., Khuvis, S., Danish, E., et al.: The Reference Elevation Model of Antarctica – Mosaics, Version 1.1, [Dataset], Harvard Dataverse, https://data.pgc.umn.edu/elev/dem/setsm/REMA/mosaic/v1.1/200m/ (last access: 15 January 2026), 2022.

Joughin I, Shapero D, Smith B, Dutrieux P, Barham M: Ice-shelf retreat drives recent Pine Island Glacier speedup. Sci Adv. ,7(24), eabg3080. doi: 10.1126/sciadv.abg3080, 2021.

325 Laffin, M. K., Zender, C. S., Singh, S., van Wessem, J. M., Smeets, C. J. P. P., and Reijmer, C. H.: Climatology and evolution of the Antarctic Peninsula foehn wind-induced melt regime, 1979–2018, J. Geophys. Res. Atmos., 126, e2020JD033682, https://doi.org/10.1029/2020JD033682, 2021.

Liu, M., Wang, Z., Zhang, B., Song, X., and An, J.: Variation in basal channels and basal melt rates of Pine Island Ice Shelf, Acta Oceanol. Sin., 43, 22–34, https://doi.org/10.1007/s13131-023-2271-x, 2024.

330 Mankoff, K. D., Jacobs, S. S., Tulaczyk, S. M., and Stammerjohn, S. E.: The role of Pine Island Glacier ice shelf basal channels in deep-water upwelling, polynyas and ocean circulation in Pine Island Bay, Antarctica, Ann. Glaciol., 53, 123–128, https://doi.org/10.3189/2012AoG60A083, 2012.

Moholdt, G. and Matsuoka, K.: Inventory of Antarctic ice rises and rumples (version 1), Norwegian Polar Institute [dataset], https://doi.org/10.21334/NPOLAR.2015.9174E644, 2015.

335 Morlighem, M.: MEaSUREs BedMachine Antarctica (NSIDC-0756, Version 3), NASA NSIDC DAAC [dataset], https://doi.org/10.5067/FPSU0V1MWUB6 (last access: 15 January 2026), 2022.

https://doi.org/10.5194/egusphere-2026-246
Preprint. Discussion started: 30 January 2026

Morlighem, M., Rignot, E., Binder, T., Blankenship, D. D., Drews, R., Eagles, G., et al.: Deep glacial troughs and stabilizing ridges unveiled beneath the margins of the Antarctic ice sheet, Nat. Geosci., 13, 132–137, https://doi.org/10.1038/s41561-019-0510-8, 2020.

Rignot, E.: Ice-shelf changes in Pine Island Bay, Antarctica, 1947–2000, J. Glaciol., 48, 247–256, https://doi.org/10.3189/172756502781831386, 2002.

Rignot, E., Mouginot, J., and Scheuchl, B.: Antarctic grounding line mapping from differential satellite radar interferometry, Geophys. Res. Lett., 38, L10504, https://doi.org/10.1029/2011GL047109, 2011.

Rignot, E., Mouginot, J., and Scheuchl, B.: MEaSUREs Antarctic Grounding Line from Differential Satellite Radar Interferometry (NSIDC-0498, Version 2), NASA NSIDC DAAC [dataset], https://doi.org/10.5067/HGLT8XB480E4 (last access: 15 January 2026), 2016.

Rignot, E., Mouginot, J., and Scheuchl, B.: MEaSUREs Grounding Zone of the Antarctic Ice Sheet (NSIDC-0778, Version 1), NASA NSIDC DAAC [dataset], https://doi.org/10.5067/HGLT8XB480E4 (last access: 15 January 2026), 2023.

Savidge, E., Snow, T., and Siegfried, M. R.: Multi-decadal record of sensible-heat polynya variability from satellite optical and thermal imagery at Pine Island Glacier, West Antarctica, Geophys. Res. Lett., 50, e2023GL106178, https://doi.org/10.1029/2023GL106178, 2023a.

Savidge, E., Snow, T., Siegfried, M. R., Zheng, Y., Bôas, A. B. V., Bortolotto, G. A., et al.: Wintertime polynya structure and variability from thermal remote sensing and seal-borne observations at Pine Island Glacier, West Antarctica, IEEE Trans. Geosci. Remote Sens., 61, 1–13, https://doi.org/10.1109/TGRS.2023.3271453, 2023b.

Schmeltz, M., Rignot, E., and MacAyeal, D. R.: Ephemeral grounding as a signal of ice-shelf change, J. Glaciol., 47, 71–77, https://doi.org/10.3189/172756501781832382, 2001.

Shean, D. E., Joughin, I. R., Dutrieux, P., Smith, B. E., and Berthier, E.: Ice shelf basal melt rates from a high-resolution digital elevation model record for Pine Island Glacier, Antarctica, The Cryosphere, 13, 2633–2656, https://doi.org/10.5194/tc-13-2633-2019, 2019.

Smith, B., Adusumilli, S., Csathó, B. M., Felikson, D., Fricker, H. A., Gardner, A., Holschuh, N., et al.: ATLAS/ICESat-2 L3A Land Ice Height, Version 6, NASA NSIDC DAAC [dataset], https://doi.org/10.5067/ATLAS/ATL06.006 (last access: 15 January 2026), 2023.

https://doi.org/10.5194/egusphere-2026-246
Preprint. Discussion started: 30 January 2026

Smith, B., Fricker, H. A., Holschuh, N., Gardner, A. S., Adusumilli, S., Brunt, K. M., et al.: Land ice height-retrieval algorithm for NASA's ICESat-2 photon-counting laser altimeter, Remote Sens. Environ., 233, 111352, https://doi.org/10.1016/j.rse.2019.111352, 2019.

Walker, C. C., Millstein, J. D., Miles, B. W. J., et al.: Multi-decadal collapse of East Antarctica's Conger–Glenzer Ice Shelf, Nat. Geosci., 17, 1240–1248, https://doi.org/10.1038/s41561-024-01582-3, 2024.

Wang, S., Alexander, P., Wu, Q., Tedesco, M., and Shu, S.: Characterization of ice shelf fracture features using ICESat-2 – a case study over the Amery Ice Shelf, Remote Sens. Environ., 255, 112266, https://doi.org/10.1016/j.rse.2020.112266, 2021.

Wild, C. T., Snow, T., Dotto, T. S., Davis, P. E. D., Tyler, S., Scambos, T. A., Pettit, E. C., and Heywood, K. J.: Thwaites Eastern Ice Shelf cavity observations reveal multiyear sea ice dynamics and deepwater warming in Pine Island Bay, West Antarctica, Ocean Sci., 21, 2605–2629, https://doi.org/10.5194/os-21-2605-2025, 2025.

Yoon, S. T., Lee, W. S., Nam, S., Lee, C. K., Yun, S., Heywood, K., et al.: Ice front retreat reconfigures meltwater-driven gyres modulating ocean heat delivery to an Antarctic ice shelf, Nat. Commun., 13, 306, https://doi.org/10.1038/s41467-021-21446-2, 2022.

Zheng, Y., Heywood, K. J., Webber, B. G. M., et al.: Winter seal-based observations reveal glacial meltwater surfacing in the southeastern Amundsen Sea, Commun. Earth Environ., 2, 40, https://doi.org/10.1038/s43247-021-00040-3, 2021.

Zhou, S., Dutrieux, P., Giulivi, C., Silvano, A., Auckland, C., Abrahamsen, P., et al.: Southern Ocean moored time series (south of 60° S) (OCEAN ICE D1.1), SEANOE [dataset], https://doi.org/10.17882/99922 (last access: 15 January 2026), 2024.

Zhou, S., Dutrieux, P., Giulivi, C. F., Jenkins, A., Silvano, A., Auckland, C., Abrahamsen, E. P., et al.: The OCEAN ICE mooring compilation: a standardised, pan-Antarctic database of ocean hydrography and current time series, Earth Syst. Sci. Data, https://doi.org/10.5194/essd-2025-54, 2025.